Biosensors and Bioelectronics 142 (2019) 111577

Contents lists available at ScienceDirect

Biosensors and Bioelectronics

journal homepage: www.elsevier.com/locate/bios

One-step electrodeposition of AuNi nanodendrite arrays as photoelectrochemical biosensors for glucose and hydrogen peroxide detection

Lanfang Wang[a,b], Weiqi Zhu[a], Wenbo Lu[a], Lina Shi[a], Rui Wang[a], Ruixue Pang[a,b], YueYue Cao[a,b], Fang Wang[a,b], Xiaohong Xu[a,b,*]

[a] Key Laboratory of Magnetic Molecules and Magnetic Information Materials of Ministry of Education, School of Chemistry and Materials Science of Shanxi Normal University, Linfen, 041004, China

[b] Research Institute of Materials Science of Shanxi Normal University & Collaborative Innovation Center for Shanxi Advanced Permanent Magnetic Materials and Technology, Linfen, 041004, China

ARTICLE INFO

Keywords:
AuNi nanodendrite arrays
One-step electrodeposition
Nonsemiconductor photoelectrochemical biosensor
Plasmonic effect

ABSTRACT

A novel nonsemiconductor photoelectrochemical biosensor was first constructed using the unique plasmonic AuNi nanodendrite arrays. The AuNi nanodendrite arrays were rapidly prepared by a one-step electrodeposition method using the porous anodic aluminum templates. Owing to its hierarchical structure with abundant active sites, the synergistic catalytic of Au and Ni can be better exploited. These plasmonic AuNi nanodendrite arrays display exceptional photoelectrocatalytic activities for glucose oxidation and hydrogen peroxide reduction reaction under visible light illumination. Specifically, the detection sensitivity for glucose ($3.7277\ mA\ mM^{-1}\ cm^{-2}$) under illumination is about 3.3 folds improvement than in the dark ($1.1287\ mA\ mM^{-1}\ cm^{-2}$), together with high accuracy and low detection limit of 3 μM. The markedly enhanced performance of AuNi nanodendrite arrays can be attributed to its hierarchical structure with abundant active sites and plasmonic effect of Au with strong absorption band in visible region. Such a newly developed method via the facile and low-cost route is of great significance in designing the plasmon-aided photoelectrochemical biosensors.

1. Introduction

Nowadays, diabetes has been a global public health problem (Danaei et al., 2011). The fluctuation in blood glucose level might result in a serious damage to various body systems, such as renal, cardiovascular, retinal, and nervous. Therefore, development of reliable and accurate quantification methods for glucose determination is of great importance in clinical and biomedical applications (Tamborlane et al., 2008). Recently, different metallic nanostructures such as platinum, gold, silver, nickel and their alloys have been explored as electrode materials to develop non-enzymatic glucose sensors (Welch and Compton, 2006; Lu et al., 2009; Lee et al., 2019). Unfortunately, the slow reaction kinetics and low sensitivity of these electrodes limits their widely applications (Ye et al., 2004). The electrocatalytic activity of the electrochemical glucose sensors is the key factor that influences both the sensitivity and selectivity of detection (Safavi et al., 2009). Therefore, development of a more active glucose sensor with a high sensitivity and selectivity is highly desired.

Plasmon induced nonsemiconductor photoelectrochemical biosensor has been considered as one of the most environment-friendly and efficient biosensor methods because of their promising performances, such as negligible background current, high sensitivity and selectivity (Wang et al., 2017a; Belushkin et al., 2018; Zhang et al., 2019). Due to their fascinating localized surface plasmon resonance (LSPR) characteristics, the plasmonic metals can harvest light at specific wavelengths and thus induce the oscillation charge carriers, which can participate in photoelectrochemical reactions (Christopher et al., 2011; Clavero, 2014; Brongersma et al., 2015; Linic et al., 2015; Zheng et al., 2015; Ding et al., 2016; Landry et al., 2017; Zhang et al., 2017c; Zhou et al., 2018). In the field of plasmon induced photoelectrocatalysis, both the activity and stability of catalysts have always been a research focus over the past decades. Such challenges can be unlocked by the innovation of the structure and morphology of the catalyst (Wang et al., 2013; He et al., 2014; Holewinski et al., 2014; Bu et al., 2016; Liu et al.,

* Corresponding author. School of Chemistry and Materials Science, Shanxi Normal University, NO.1, Gongyuan Street, Linfen, Shanxi, 041004, PR China.
E-mail address: xuxh@sxnu.edu.cn (X. Xu).

https://doi.org/10.1016/j.bios.2019.111577
Received 9 May 2019; Received in revised form 27 July 2019; Accepted 6 August 2019
Available online 09 August 2019
0956-5663/

2016; Kim et al., 2017; Zhang et al., 2017b; Yin et al., 2018). Among the various structures, binary nanodentrites with interconnected branches are considered as an excellent candidate for photoelectrocatalysis due to their high surface reaction sites and high density "hot spots" for efficient charge separation and transport (Wang et al., 2015; Choi et al., 2016; Naveen et al., 2016; Balram et al., 2017; Zhang et al., 2017a). Such binary nanodentrites usually exhibit better catalytic activities than their single composition because of the synergistic effects of multiple compositions (Hsu & Wang et al., 2014). Binary nanostructures have been widely used in nonenzymatic glucose sensors because of their significant features, such as high surface area, rapid mass transport, high catalytic efficiency as well as biocompatibility. To date, several methods have been developed for the fabrication of binary nanodentrites, including underpotential deposition, hydrothermal-assisted seed growth and electrochemical dealloying (Wang et al., 2016, 2017b; Benn et al., 2017; Cui et al., 2017; Guo et al., 2017; Nguyen et al., 2019; Zhang et al., 2019). Among of which, underpotential deposition have received much attention because of the benefits of being simple, eco-friendly, and easy to operate (Li et al., 2013). Unfortunately, for the binary nanodentrites usually supported on carbon electrode or other conducting substrate, it is inevitable that they typically suffer from inadequate stability because of the corrosion of carbon or Ostwald agglomeration of the nanodentrites (Stamenkovic et al., 2006). To overcome these disadvantages, we examined the porous anodic aluminum (PAA) templates during the underpotential deposition process to separate binary nanodentrites to form nanodentrite arrays. These arrays show much better durability because of their inherent structural stability, which is similar in structure to nanowire arrays. However, to date, there are few reports that binary nanodentrites separated with the porous anodic aluminum (PAA) template have been used as the plasmon induced nonsemiconductor photoelectrochemical biosensor.

Binary nanodentrites are interesting because integration of a plasmonic part and a catalytic part is simple (Yang et al., 2015, 2016; Lee et al., 2017a; Lin et al., 2017). As a popular noble metal, Au not only exhibits unique plasmonic effect but also has the electrocatalytic activity for glucose oxidation and hydrogen peroxide reduction (Chen et al., 2012; Yan et al., 2016; Zheng et al., 2016; Wang et al., 2017a, 2018b; Baek et al., 2018; Lee et al., 2019). However, the high cost and surface poisoning effect have limited its practical applications. Nickel-based materials with high oxidation activity for glucose have been widely used to fabricate non-enzymatic electrochemical glucose sensors (Lu et al., 2009; Hsu and Wang, 2014). Therefore, the combination of Au and Ni will predictably pull down the high cost of Au and realize the synergistic integration of a plasmonic function and a catalytic function. Moreover, due to its multiple high angle edges and sharp tips, the formation of hierarchical structure plays an important role to improve the electrocatalytic activity for glucose and H_2O_2 detection (Naveen et al., 2016; Guo et al., 2017). Unfortunately, plasmon induced nonsemiconductor photoelectrochemical biosensor based on AuNi binary nanodentrites for detecting glucose and hydrogen peroxide have not been reported.

In this article, we present a one-step electrodeposition method using the porous anodic aluminum templates to rapidly synthesize the AuNi nanodendrite arrays (NDAs) for the first time. The as-prepared AuNi NDAs display strong LSPR peaks in the visible region and outstanding photoelectrocatalytic activities for glucose oxidation and hydrogen peroxide reduction reaction. The detection sensitivity for glucose under illumination is about 3.3 folds improvement than in the dark, together with low detection limit, high accuracy and good selectivity. By comparing with the AuNi alloy nanowires (ANWs) and AuNi/Au multilayered nanowires (MNWs), the abundant active sites of AuNi NDAs and plasmonic effect of Au are responsible for the markedly photoelectrocatalytic activity.

2. Experimental

2.1. Chemicals

Gold (III) chloride hydrate ($HAuCl_4{\cdot}4H_2O$) was obtained from Alfa Aesar. Nickel sulfate ($NiSO_4{\cdot}6H_2O$), boric acid (H_3BO_3), glucose, hydrogen peroxide (H_2O_2), uric acid (UA), ascorbic acid (AA), L-tyrosine, xylose, maltose, galactose, lactose and fructose of analytical reagent grade were purchased from Aladdin Chemical Co. Ltd. The conductive Indium Tin Oxide (ITO) substrates were obtained from the Hefei Kejing Materials Technology Co., Ltd. Deionized water was used throughout our experiments.

2.2. Preparation of AuNi NDAs and modified electrode

The AuNi NDAs were fabricated by a one-step electrodeposition method using the PAA templates (pore diameter is 70 nm). The electrolyte is made up of 2 M $NiSO_4$, 4 mM $HAuCl_4$ and 0.5 M H_3BO_3. According to our previous study, the PAA template sputtered with a Au layer of 150 nm was served as the working electrode (Wang et al., 2018a, 2018b). A potentiostatic pulse deposition consisted of two deposition steps of −0.75 V for 1 s and 0 V for 1 s was carried out to deposit AuNi. The pulse cycles are 300. During the deposition steps, the relaxation time of 1 s at 0 V was designed to make the ions have enough time to travel near the deposition sites. In this process, various deposition potentials (−0.5 V, −0.7 V, −0.75 V, −0.8 V and −1 V) were used to prepare nanostructures with different surface morphologies. After deposition, a modified electrode was prepared by attaching the PAA templates with the AuNi nanostructures on the surface of ITO substrate. Then the uncoated ITO surface was covered by an epoxy resin for insulation. Subsequently, the PAA membrane was etched away in 0.5 M H_3PO_4 solution for 60 min. For comparison, the AuNi ANWs and AuNi/Au MNWs were also fabricated in a parallel conditions but using the different deposition potentials. The AuNi ANWs were deposited at −1.2 V for 300 s. The AuNi/Au MNWs were deposited at −1.2 V for 2 s and −0.5 V for 1 s to prepare AuNi layer and Au layer, respectively.

2.3. Apparatus and photoelectrochemical measurements

Surface morphology, microstructure and crystal structure of the prepared AuNi nanostructures were investigated by scanning electron microscope (SEM), transmission electron microscopy (TEM) and X-ray Diffraction (XRD). To prepare the TEM samples, the AuNi NDAs were detached totally from the PAA templates through dipping the template in 1 M NaOH solution for 60 min, and then the AuNi NDAs were dispersed in ethanol through ultrasonic oscillations. For transmission electron microscopy (TEM) characterizations, small drops of the suspended solution were placed on a TEM grid and finally allowing the solvent to evaporate. After that, we measured the TEM images of the samples on the TEM grid. The composition and chemical valence state were examined by energy-dispersive X-ray spectroscopy (EDX) and X-ray photoelectron spectroscopy (XPS). All the binding energies for XPS spectra were corrected by using C 1s line at 284.8 eV. The content of Ni were characterized by magnetic hysteresis loops ($M-H$), which were obtained from superconducting quantum interference device (SQUID). The ultraviolet–visible (UV–vis) absorption spectrum was performed in the wavelength range of 400–800 nm. The potentiostatic pulse deposition, the photoelectrochemical measurements were performed using an IM6e electrochemical workstation. All the manipulations were carried out at ambient temperature (26 ± 1 °C). The photoelectrochemical cell was assembled with a modified electrode (working electrode), a Pt wire electrode (counter electrode), an Ag/AgCl electrode (reference electrode) and an analyst solution. The visible light ($\lambda > 400$ nm) was illuminated on the front side of the AuNi NDAs biosensor by using a 300 W xenon lamp system. The lamp was placed 10 cm away from the photoelectrochemical cell.

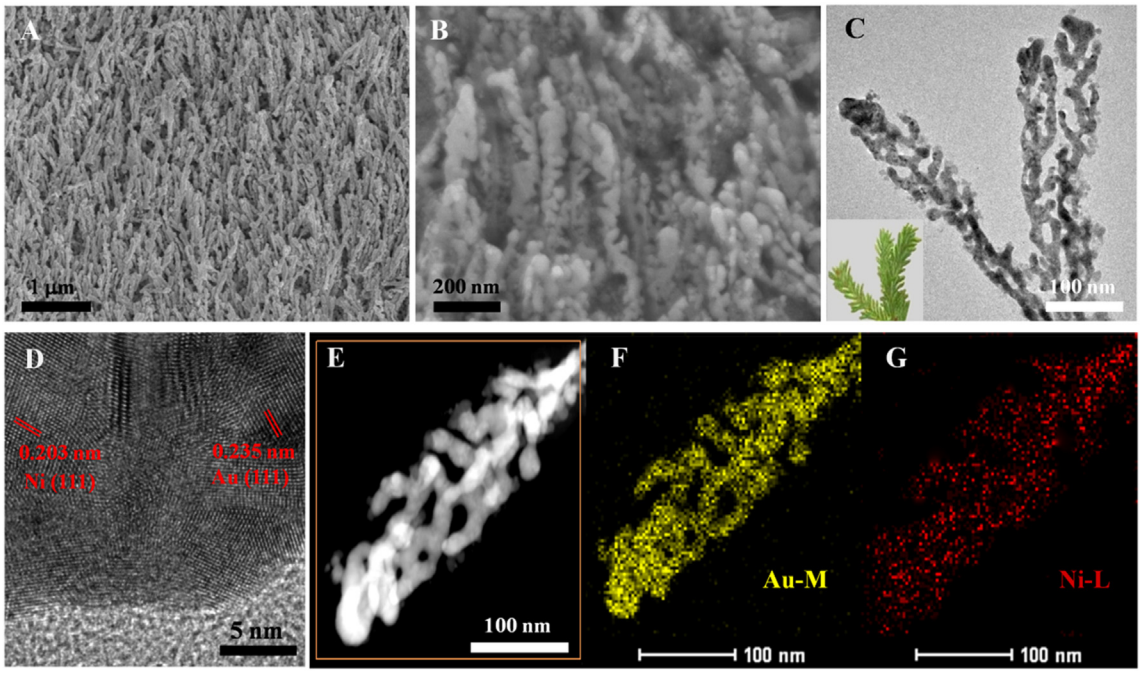

Fig. 1. (A) TEM image for the AuNi NDAs synthesized with deposition potential of −0.75 V. (B) HRTEM image of the AuNi NDAs. (C) HAADF-STEM image of a single representative AuNi NDAs and elemental maps of Au (D) and Ni (E).

3. Results and discussion

3.1. Characterization of the synthesized AuNi NDAs

SEM measurement was performed to characterize the surface morphology of the prepared AuNi NDAs. Fig. 1A−B displays the typical SEM image of the AuNi NDAs synthesized with the deposition potential of −0.75 V. It is evident that the AuNi NDAs are vertically aligned and the branch is multitude. From the detailed EDX data in Fig. S1, it can be seen that the Au and Ni content is obviously present and the atomic ratio of Au and Ni in AuNi NDAs is about 38:1. The micro-morphology of samples was investigated by TEM, as shown in Fig. 1C. It is clearly observed that AuNi NDAs consist of a number of densely packed branches, like “pine leaves”, as shown in the inset of Fig. 1C. These hierarchical dendrites provide a higher surface-to-volume ratio and abundant active sites. Fig. S2A−D displays the SEM images of the nanostructures fabricated with different deposition potentials. It was clearly that the morphology of nanostructures has a strong dependence on the deposition potential. When the redox potential is high, the nanostructures consist of nanoparticles. While the redox potential is low, the nanostructures are smooth nanowires. Only when the deposition potential is −0.75 V, the AuNi NDAs with interconnected branches were obtained. The formation of dendritic structure may be due to the underpotential deposition of Ni (Qu et al., 2016; Guo et al., 2017). The crystalline nature of the AuNi NDAs can be analyzed from the high-resolution TEM (HRTEM) image. As shown in Fig. 1D, highly ordered crystallographic fringes are clearly observed. The spacing of 0.235 nm and 0.203 nm between the lattice fringes are corresponded to the Au (111) and Ni (111), respectively. Fig. 1E shows the high angle annular dark field scanning TEM (HAADF-STEM) image of the AuNi NDAs. A direct visual inspection of the element distribution for AuNi NDAs was obtained from the energy dispersive X-ray spectroscopy (EDS) mapping experiments. As shown in Fig. 1F−G, the distribution of Au and Ni is quite uniform in the AuNi NDAs, demonstrating their bimetallic nature. According to the location and intensity, the Au and Ni elements are intermixing of each element. These results combined demonstrate that the AuNi NDAs were successfully and rapidly prepared using the developed one-step electrodeposition method.

Fig. 2Ashows the XRD patterns of the AuNi NDAs. The characteristic diffraction peaks centered at 38.2, 44.3 and 64.6 are attributed to the (111), (200) and (220) planes of Au. Diffraction peaks located at 44.4 and 51.8 are corresponded to Ni (111) and Ni (200) planes, respectively. Fig. 2B displays the $M-H$ curves of the prepared AuNi NDAs, in which the applied magnetic field are parallel and perpendicular to the nanostructure axis. The curve reveals that the AuNi NDAs have no obvious easy axis direction. Further, the coercivities for the AuNi NDAs in both parallel and perpendicular directions are very small. It may be because that the Ni nanostructures with small size are superparamagnetic and low magnetocrystalline anisotropy (Zhang et al., 2014). As mentioned above, the AuNi NDAs are made of hierarchical dendrites, and the average diameter of the dendrites is about 20 nm. Thus the weak coupling along the nanostructure axis makes the dendrites barely ferromagnetic, with very small coercivity and remanence. $M-H$ curves of the AuNi nanostructures prepared with different potentials (−0.5 V, −0.7 V, −0.8 V, −1 V) are shown in the Fig. S3A−D. The coercivity and remanence are increased with the increase of the depostition potentials, consequently resulting in the great increase of Ni content. These results highlight that the Au/Ni atomic ratio of the AuNi nanostructures is adjusted by the deposition potentials. Thus, the deposition potential and the content of Ni have a significant influence on the morphology of the resulting binary nanostructures.

The surface chemical composition and valence state of the AuNi NDAs are detected by XPS spectra. As shown in Fig. S4, the overview survey spectrum clearly shows all of the anticipated elements (C, O, Ni and Au elements), corresponding with the EDX spectrum results (Fig. S1). In the Ni 2p XPS spectrum (Fig. 2C), two peaks centered at 852.7 and 870.2 eV correspond to the metallic Ni. Since the Ni nanostructures are susceptible to oxidation, two characteristic peaks occur at 855.5 and 873.2 eV are attributed to the main peaks of oxidized Ni $2p_{3/2}$ and Ni $2p_{1/2}$, respectively. Correspondingly, the two peaks of 861.3 and 880 eV are the satellite peaks of the oxidized Ni. The Au 4f spectrum (Fig. 2D) can be fitted to two major peaks at 87.57 and 83.97 eV, which corresponds to the zero valence Au^0. Compared to the pure Au (84 and 87.7 eV), the Au 4f binding energies of AuNi NDAs show a little shift to the lower value, which indicates the electron may transfer from Ni to Au and a strong interaction between Au and Ni (Cui et al., 2017).

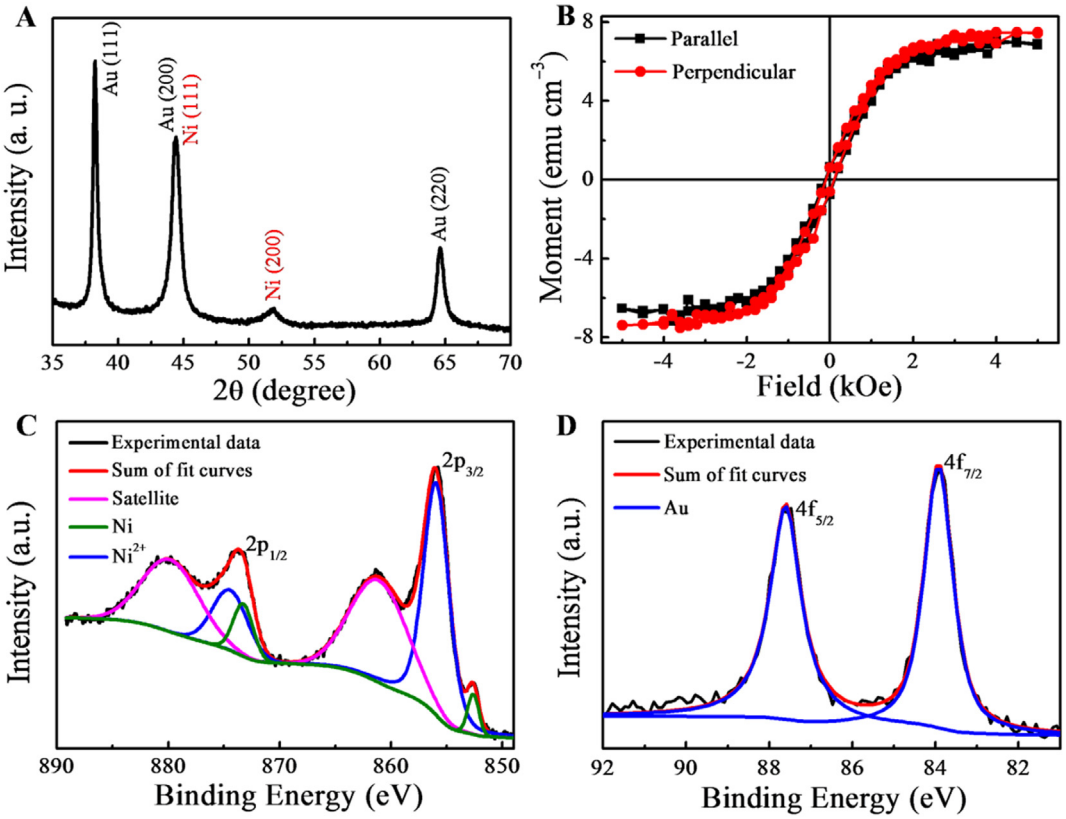

Fig. 2. (A) XRD curve and (B) $M-H$ curves of the AuNi NDAs. XPS spectrum of (C) Ni 2p and (D) Au 4f in AuNi NDAs.

3.2. Photoelectrochemical properties of AuNi NDAs for glucose

The absorption spectra of the AuNi ANWs, AuNi/Au MNWs and AuNi NDAs are included in Fig. 3A. Compared with the AuNi ANWs, the AuNi NDAs and AuNi MNWs present obvious absorption in the visible region. These absorption peaks of the AuNi NDAs and AuNi MNWs are located at around 540 nm, revealing that the absorptions could be originated from the plasmonic effect of Au nanoparticles. The absorption peak of AuNi NDAs is obviously blue-shift compared to that of the AuNi MNWs, indicating the electronic interactions between Au and Ni. Thus, this strong light trapping of the AuNi NDAs should ascribe to both of the hierarchical structure and the plasmonic effect of Au nanoparticles. The electrocatalytic activity of AuNi NDAs for glucose oxidation was performed in NaOH solution (0.2 M). As seen from Fig. 3B, the cyclic voltammetry (CV) curve of AuNi NDAs electrode gives a pair of redox peak with anodic peak at about 0.38 V and cathodic peak at about 0.03 V. After adding 10 mM glucose into the NaOH solution, anodic current peaks in both the forward and reverse potential scans remarkably increase, indicating the good electrocatalytic for glucose oxidization.

To investigate the influence of plasmonic effect on the electrocatalytic for glucose oxidization, the photocurrent responses in absence/presence of 10 mM glucose at 0.4 V with visible light switching ON and OFF was shown in Fig. 3C. When visible light was ON condition, AuNi NDAs electrode in NaOH solution displayed a low photocurrent response. While 10 mM glucose was injected to the electrolytic solution, the photocurrent response was dramatically increased. This pronounced increase reveals that the glucose may initiates the separation of hot electrons and hot holes. For comparison, control experiments of AuNi ANWs and AuNi MNAs were also performed. As displayed in Fig. S5A – D, the photocurrent response with presence of glucose under similar conditions exhibited a lower value. This indicates that the photoelectric conversion efficiency in AuNi NDAs is improved because of the unique nanodendrite structure. Besides, to generate a high photocurrent response on the glucose sensor, the variable deposition conditions such as the concentration of $HAuCl_4$ in the supporting electrolyte and the electrodeposition potentials were optimized. As displayed in Fig. S6A – B, the enhanced current density (Δj) with the deposition electrolyte of 4 mM $HAuCl_4$ and the deposition potential of −0.75 V is the largest. These results combined with the SEM images (Fig. S2A – D) indicate that the efficient plasmon-enhanced electrocatalytic glucose oxidization could be realized by constructing an appropriate atom ratio of AuNi NDAs. And the unique nanodendrite structure provides a large surface area as the active place for light confinement and catalytic reaction sites. Based on above results, schematic illustration for the visible light-driven glucose oxidation on the AuNi NDAs electrode is shown in Fig. 3D. Upon illumination by visible light, the incorporation of plasmonic effect of Au may facilitate the separation of hot carriers (electrons-holes) on the AuNi surface. These nanodendrite nanostructures enable intimate contact between the electrolyte and the AuNi NDAs surface, even at the bottom. This results in shorter holes diffusion distances to the electrolyte. Under a suitable potential bias, the glucose likely serves as the holes scavenger and lead to more efficient electron/hole separation, eventually resulting in an obvious enhanced photocurrent response. In addition, the vertical alignment of the AuNi NDAs aids electron transport to the ITO without a large recombination loss. Therefore, the improved catalytic performance for glucose in the AuNi NDAs is ascribed to the efficient electrons and holes transport/separation in the unique nanodendrite structure.

To further study the influence of plasmonic effect on the catalytic activity, we used linear sweep voltammogram (LSV) curves to systemically reveal the influence of the illuminating time on the catalytic activity of AuNi NDAs electrode (Fig. 4A). Evidently, the anodic peak current densities of the AuNi NDAs increase gradually until 70 min and then nearly keep constant. This increase can be ascribed to the

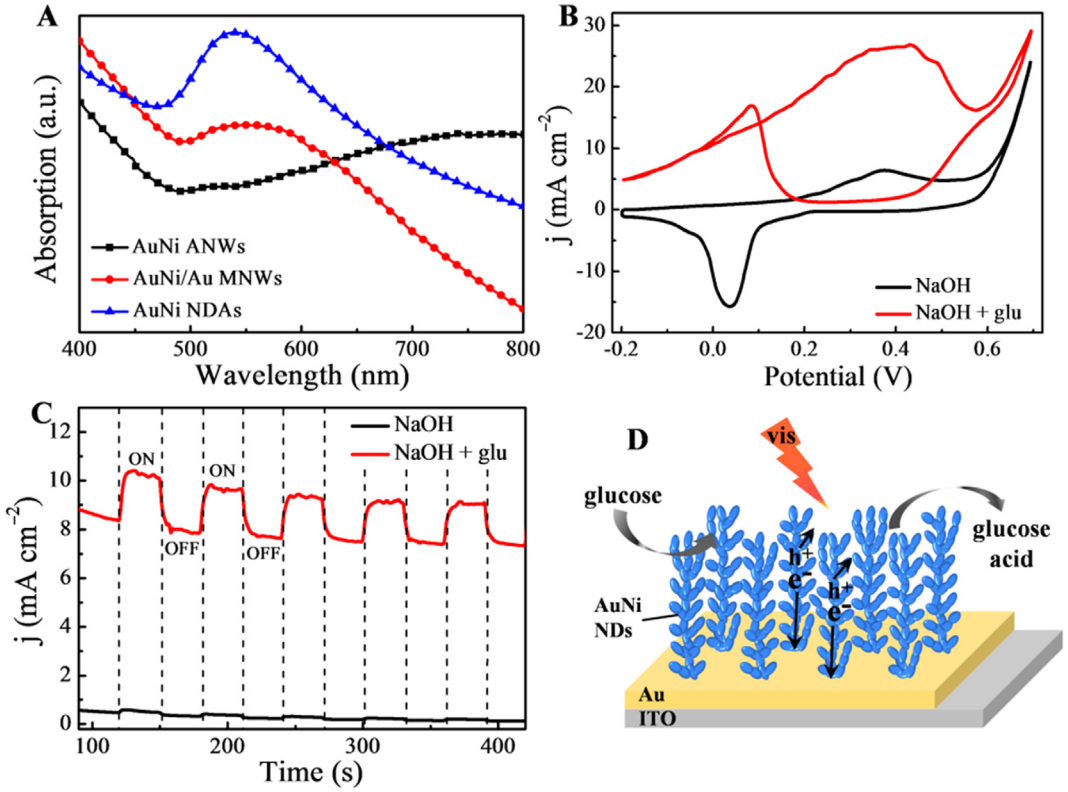

Fig. 3. (A) UV − vis absorption spectra for the AuNi ANWs, AuNi/Au MNWs and AuNi NDAs. (B) CVs of AuNi NDAs electrode in the absence and presence of 10 mM glucose. (C) $i-t$ responses of AuNi NDAs electrode with visible light switching ON and OFF. (D) Schematic illustration for the visible light-driven glucose oxidation on the AuNi NDAs electrode.

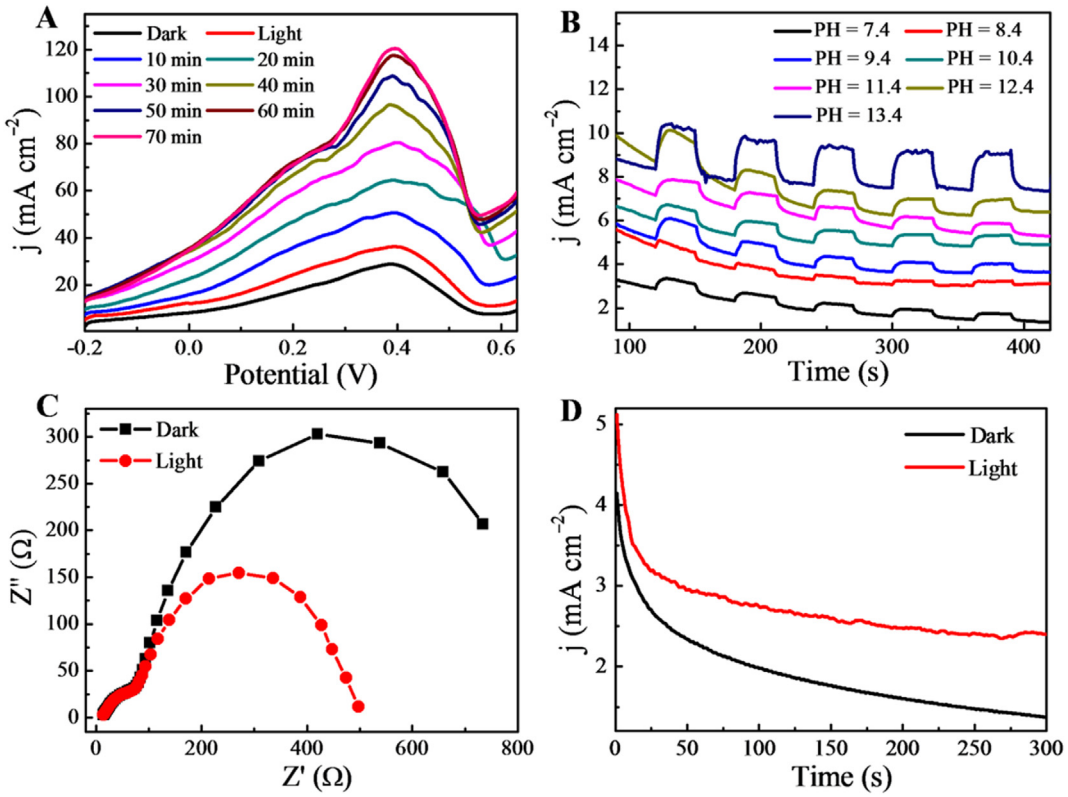

Fig. 4. (A) Influences of illuminating time on the catalytic activity of the AuNi NDAs electrode for glucose oxidization. (B) Influence of the solution pH on photocurrent response with visible light switching ON and OFF. (C) EIS curve of the AuNi NDAs electrode with visible light switching ON and OFF. (D) Long-term $i-t$ curves upon irradiation ON and OFF.

plasmonic effect of Au and the increased temperature of the solution under the irradiation. During these processes, the plasmonic photothermal and photoelectrocatalytic conversion are responsible to enhance the chemical reactions (Yang et al., 2015; Lee et al., 2017b). Accordingly, the electrocatalytic activities of AuNi NDAs gradually increase as the irradiation time increase, demonstrating that plasmon-enhanced photoelectrocatalysis under visible light irradiation can be realized. The influence of the solution pH on the enhanced current density (Δj) was investigated with visible light switching ON and OFF. As displayed in Fig. 4B, the photocurrent response increases gradually when the solution pH increases from 7.4 to 13.4. It may be because that glucose is easily oxidized at high pH (Lu et al., 2009). In highly alkaline conditions, more hydroxyl anions (OH^-) in highly alkaline conditions can directly participate in the oxidization of Au/Ni to form AuOH/NiOOH. Then the AuOH and NiOOH catalyze glucose oxidation to glucose acid. Accordingly, more hot holes can be captured in highly alkaline conditions than that in neutral conditions, resulting in a much larger Δj (Wang et al., 2017a). In addition, electrochemical impedance spectroscopy (EIS) (Fig. 4C) exhibit that the AuNi NDAs electrode upon visible light irradiation have lower charge transfer resistance compared with that in the dark. This leads to a faster reaction rate for glucose oxidization. The significant decrease of charge-transfer resistance could be attributed to the unique nanodendrite structure and plasmonic effect of Au. In addition to activity, stability is another key parameter to evaluate the property of glucose electrocatalysts. In order to evaluate the poisoning effect originated from the adsorption of reaction product (glucose acid) on Au surface, long-term $i-t$ curves upon irradiation ON and OFF were obtained at 0.4 V. As evident from Fig. 4D, the AuNi NDAs electrode upon irradiation shows an initial higher current density along with less current decay. These results indicate that the poisoning effect can be alleviated using the plasmonic effect of Au.

3.3. Catalytic performance, selectivity, stability and real sample analysis of AuNi NDAs glucose sensor

To further evaluate the catalytic performance of the AuNi NDAs glucose sensor, $i-t$ curve upon irradiation ON and OFF was performed to reveal the current responses to glucose. Under the above optimized conditions, Fig. 5A records the current responses of the AuNi NDAs electrode through successive injection of glucose into constantly stirred 0.2 M NaOH solution. Inset of Fig. 5A displays the enlarged $i-t$ curve from 300 to 550 s, as is marked by the blue rectangle. It is clear that the response current increased rapidly after each injection of glucose and arrived at a steady state within 10 s. This can be illustrated by the fast electron transfer between the glucose and electrode. And the increase of response current for the electrode under the irradiation is more. The current signals change with glucose concentration are summarized and plotted in Fig. 5B. The linear regression equations under irradiation were I (mA cm^{-2}) = 3.7277$C_{glucose}$ + 0.412 in the range of 0.005–15 mM, and that in the dark were I (mA cm^{-2}) = 1.1287 $C_{glucose}$ + 0.587 in the range of 0.01–13 mM, respectively. It is obvious that the sensitivity of 3.7277 mA mM^{-1} cm^{-2} obtained under irradiation is 3.3 fold higher than that in the dark (1.1287 mA mM^{-1} cm^{-2}). Besides, the detection limit under irradiation (3 μM) is better than that in dark (5 μM). The lower detection limit should be ascribed to the higher detection sensitivity. Compared with some other non-enzymatic glucose sensors based on Au-based and Ni-based materials (Table S1), the AuNi NDAs electrode under irradiation prepared in this work have an ultrahigh sensitivity, wide linear range and low detection limit.

We also evaluate the selectivity and stability of the amperometric glucose sensor. The oxidizable compounds such as hydrogen peroxide (H_2O_2), uric acid (UA), ascorbic acid (AA), L-tyrosine, xylose, maltose, galactose, lactose and fructose are normally co-existed with glucose in real samples. Interference of these compounds can degrade the detection efficacy of glucose sensor (Lu et al., 2009; Bernstein et al., 2013). Therefore, it is necessary to add some interference substances to investigate the anti-interference performance of the AuNi NDAs sensor. Due to the physiological levels of interfering substances (< 0.1 mM) are less than the glucose (3–8 mM), we measured the response current of this sensor with the addition of 2 mM glucose and 0.05 mM interfering substances (Zhang et al., 2008). The amperometric response was recorded at 0.4 V to evaluate the selectivity by successive injection of interfering substances and glucose into 0.2 M NaOH solution. As shown in Fig. 5C, the results show only a small change to the injection of interfering substances, which can be negligible. This indicates that the system is less sensitive to the interfering substances. The excellent selectivity of the AuNi NDAs electrode can be as a result of the low applied potential and the nanodentric structure. The repeatability is investigated by three successive amperometric responses and the RSD is less than 4.5%. Long-term stability was tested at 5 days intervals. Fig. 5D shows that the amperometric response of AuNi NDAs electrode decreases to 93% after 30 days, which indicates that the sensor has good stability.

The accuracy of the sensor was evaluated by determining the glucose concentration by using this method. The human blood serum samples were obtained from healthy men (n = 3). When human serum was spiked into 0.2 M NaOH solution with volume ratio 1:100, amperometric studies were performed using the AuNi NDAs electrode to detect the content of glucose in human serum samples. The results from three times measurements for each sample were compared with that from the commercially available glucometer (ACCU-CHEK ACTIVE, Roche Diagnostics GmbH, Germany) as shown in Table S2. It can be seen that the calculated content of glucose using AuNi NDAs is acceptable by comparison with the commercial glucometer.

3.4. Catalytic performance of AuNi NDAs biosensor for H_2O_2

Besides the electrochemical oxidation of glucose, the electrochemical reduction of H_2O_2 was also investigated to demonstrate the superior bifunctional catalytic activities of AuNi NDAs. Fig. 6A shows the CVs for the H_2O_2 reduction on the AuNi NDAs electrode in 0.1 M phosphate-buffered saline (PBS, PH = 7.4). When 5 mM of H_2O_2 is added to the solution, the electrode shows a lower reduction current at a constant potential (−0.2 V) than that without H_2O_2, indicating the electrocatalytic for H_2O_2. As shown in Fig. 6B, the $i-t$ curve of photocurrent response upon irradiation ON and OFF was used to evaluate the sensitivity of the AuNi NDAs electrode for H_2O_2 detection. Under light and dark conditions, the photocurrent response of AuNi NDAs electrode was quite stable. Consequently, the current density changed periodically with light ON and OFF. Furthermore, the photocurrent response in the presence of H_2O_2 is larger than that absence of H_2O_2, demonstrating the superior catalytic activities of AuNi NDAs for H_2O_2 reduction. Fig. 6C shows *i–t* curves of the AuNi NDAs electrode upon the successive injection of H_2O_2 into the stirring PBS solution at −0.2 V. Inset is the enlarged amperometric current response from 300 to 550 s, as is marked by the blue rectangle. With each addition of H_2O_2, the electrode responded very quickly both under the irradiation and in the dark. The current reaches a steady state within a fast rate of 5 s, which could be attributed to the easy diffusion of H_2O_2 to the hierarchical nanodenticte arrays. Significantly, under visible light irradiation, the current densities increase much more upon the addition of H_2O_2, indicating the efficient electron/hole separation. The response current is plotted as a function of H_2O_2 concentration in Fig. 6D. Both under irradiation and in the dark, the AuNi NDAs electrode displays a linear current response in the range of 0.005–15 mM. The corresponding calibration curve displays a detection sensitivity of 994 μA mM^{-1} cm^{-2} under irradiation. On the contrary, the sensor shows a lower detection sensitivity of 646 μAcm^{-2} mM^{-1} in the dark. The detection limit for H_2O_2 is 2 μM and 5 μM under irradiation and in the dark, respectively. The linear regression equations under irradiation and in the dark are displayed in S7 of the Supporting Information. The results suggest that the plasmonic effect plays a significant role in the

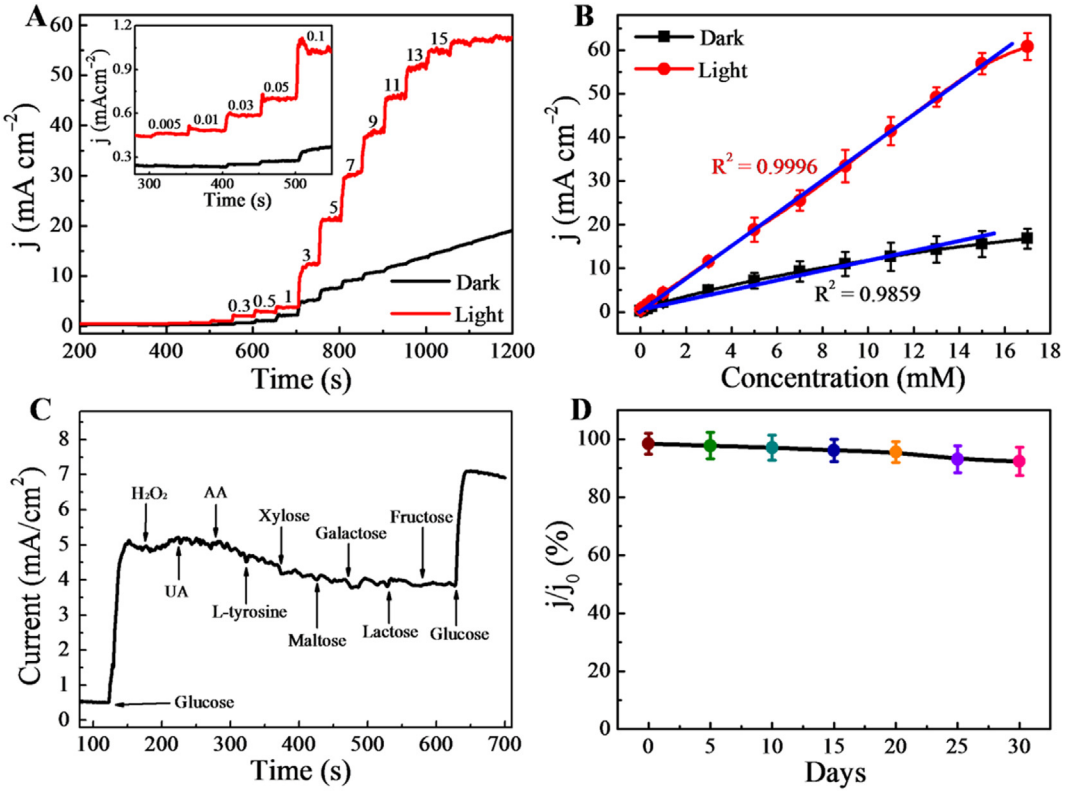

Fig. 5. (A) $i-t$ response curve of the AuNi NDAs sensor to different concentration of glucose. (B) Corresponding calibration plot of current signals change with glucose concentration under irradiation and in dark condition. Error bar: n = 3. (C) $i-t$ responses to the successive addition of interfering substances. (D) Long-term stability of the developed sensor.

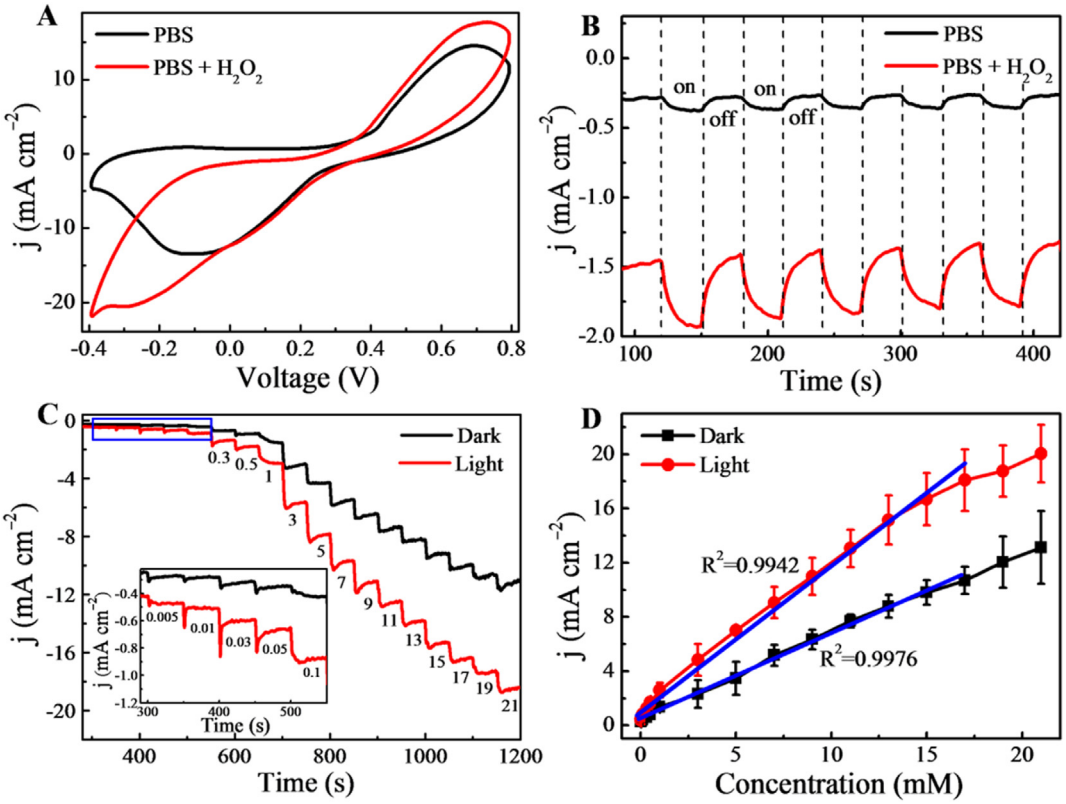

Fig. 6. (A) CV curves for AuNi NDAs electrode in the absence and presence of 5 mM H_2O_2 in PBS solution. (B) $i-t$ responses of the AuNi NDAs electrode with visible light switching ON and OFF. (C) $i-t$ response curve of the AuNi NDAs sensor to different concentration of H_2O_2. (D) The response current plotted as a function of H_2O_2 concentration. Error bar: n = 3.

enhancement of the sensitive for H_2O_2 detection.

4. Conclusion

A one-step electrodeposition method using the PAA templates was developed to rapidly grow novel AuNi NDAs arrays for the first time. These AuNi NDAs electrode show the better catalytic performance for glucose oxidation and hydrogen peroxide reduction reaction than the AuNi alloys and AuNi multilayered nanowires. Specifically, the detection sensitivity for glucose and hydrogen peroxide under illumination is improved than that in dark. The high specific surface area, abundant active sites and plasmonic effect of Au ensure its remarkable plasmon-aided photocatalytic activity, due to the strong absorption band in the visible region and effective electron/hole separation. The experimental findings reveal that the controlled assembly of bimetal nanodendrites is an effective method for the synergistic integration of plasmonic and catalytic functions into a single platform. Thus, we believe that the given photoelectrochemical biosensor fabricated from the facile and low-cost process is a promising route for extending the other photoelectrochemical biosensors.

CRediT authorship contribution statement

Lanfang Wang: Writing - original draft, Writing - review & editing. **Weiqi Zhu:** Formal analysis. **Wenbo Lu:** Investigation. **Lina Shi:** Methodology. **Rui Wang:** Methodology. **Ruixue Pang:** Validation. **YueYue Cao:** Validation. **Fang Wang:** Software. **Xiaohong Xu:** Supervision.

Acknowledgments

This work was supported by National Key R&D Program of China (No. 2017YFB0405703), the National Science Foundation of China (Grant No. 61434002, 51871137, 21705103) and the Applied Basic Research Project of Shanxi Province (No. 201801D221392).

Appendix A. Supplementary data

Supplementary data related to this article can be found at https://doi.org/10.1016/j.bios.2019.111577.

References

Baek, K.M., Kim, J., Kim, S., Cho, S.H., Jang, M.S., Oh, J., Jung, Y.S., 2018. Chem. Mater. 30, 6183–6191.
Balram, A., Zhang, H., Santhanagopalan, S., 2017. ACS Appl. Mater. Interfaces 9, 28355–28365.
Belushkin, A., Yesilkoy, F., Altug, H., 2018. ACS Nano 12, 4453–4461.
Benn, E.E., Gaskey, B., Erlebacher, J.D., 2017. J. Am. Chem. Soc. 139, 3663–3668.
Bernstein, R., Parkes, J.L., Goldy, A., Brown, D., Harrison, B., Chu, A., Pflug, B.K., Simmons, D.A., Pardo, S., Bailey, T.S., 2013. J. Diabetes Sci. Technol. 7 (5), 1386–1399.
Brongersma, M.L., Halas, N.J., Nordlander, P., 2015. Nat. Nanotechnol. 10, 25–34.
Bu, L., Guo, S., Zhang, X., Shen, X., Su, D., Lu, G., Zhu, X., Yao, J., Guo, J., Huang, X., 2016. Nat. Commun. 7, 11850.
Chen, W., Cai, S., Ren, Q.Q., Wen, W., Zhao, Y.D., 2012. Analyst 137, 49–58.
Choi, K.H., Jang, Y., Chung, D.Y., Seo, P., Jun, S.W., Lee, J.E., Oh, M.H., Shokouhimehr, M., Jung, N., Yoo, S.J., Sung, Y.E., Hyeon, T., 2016. Chem. Commun. 52, 597–600.
Christopher, P., Xin, H., Linic, S., 2011. Nat. Chem. 3, 467–472.
Clavero, C., 2014. Nat. Photonics 8 (2), 95.
Cui, X., Xiao, P., Wang, J., Zhou, M., Guo, W., Yang, Y., He, Y., Wang, Z., Yang, Y., Zhang, Y., Lin, Z., 2017. Angew. Chem. 56, 4488–4493.
Danaei, G., Finucane, M.M., Lu, Y., Singh, G.M., Cowan, M.J., Paciorek, C.J., Lin, J.K., Farzadfar, F., Khang, Y.-H., Stevens, G.A., 2011. Lancet 378 (9785), 31–40.
Ding, S.Y., Yi, J., Li, J.F., Ren, B., Wu, D.Y., Panneerselvam, R., Tian, Z.Q., 2016. Nat. Rev. Mater. 1, 16021.
Guo, L., Huang, L.B., Jiang, W.J., Wei, Z.D., Wan, L.J., Hu, J.S., 2017. J. Mater. Chem. 5, 9014–9021.
He, R., Wang, Y.C., Wang, X., Wang, Z., Liu, G., Zhou, W., Wen, L., Li, Q., Wang, X., Chen, X., Zeng, J., Hou, J.G., 2014. Nat. Commun. 5, 4327.
Holewinski, A., Idrobo, J.C., Linic, S., 2014. Nat. Chem. 6, 828–834.
Hsu, C.W., Wang, G.J., 2014. Biosens. Bioelectron. 56, 204–209.
Kim, C., Suh, B.L., Yun, H., Kim, J., Lee, H., 2017. ACS Catal. 7, 2294–2302.
Landry, M.J., Gellé, A., Meng, B.Y., Barrett, C.J., Moores, A., 2017. ACS Catal. 7, 6128–6133.
Lee, S., Lee, Y.W., Ahn, H., Kim, J.H., Han, S.W., 2017a. Curr. Opin. Electrochem. 4 (1), 11–17.
Lee, S., Wy, Y., Lee, Y.W., Ham, K., Han, S.W., 2017b. Small 13 (43), 1701633.
Lee, W.C., Kim, K.B., Gurudatt, N.G., Hussain, K.K., Choi, C.S., Park, D.S., Shim, Y.B., 2019. Biosens. Bioelectron. 130, 48–54.
Li, G.R., Xu, H., Lu, X.F., Feng, J.X., Tong, Y.X., Su, C.Y., 2013. Nanoscale 5 (10), 4056–4069.
Lin, S.C., Hsu, C.S., Chiu, S.Y., Liao, T.Y., Chen, H.M., 2017. J. Am. Chem. Soc. 139, 2224–2233.
Linic, S., Aslam, U., Boerigter, C., Morabito, M., 2015. Nat. Mater. 14, 567–576.
Liu, K., Bai, Y., Zhang, L., Yang, Z., Fan, Q., Zheng, H., Yin, Y., Gao, C., 2016. Nano Lett. 16, 3675–3681.
Lu, L.M., Zhang, L., Qu, F.L., Lu, H.X., Zhang, X.B., Wu, Z.S., Huan, S.Y., Wang, Q.A., Shen, G.L., Yu, R.Q., 2009. Biosens. Bioelectron. 25, 218–223.
Naveen, M.H., Gurudatt, N.G., Noh, H.B., Shim, Y.B., 2016. Adv. Funct. Mater. 26, 1590–1601.
Nguyen, N.A., Nguyen, T.T.T., Nguyen, V.T., Ali, Y., Sim, E., Choi, H.S., 2019. Catal. Today. https://doi.org/10.1016/j.cattod.2019.03.019.
Qu, X., Cao, Z., Zhang, B., Tian, X., Zhu, F., Zhang, Z., Jiang, Y., Sun, S., 2016. Chem. Commun. 52 (24), 4493–4496.
Safavi, A., Maleki, N., Farjami, E., 2009. Biosens. Bioelectron. 24 1655–1600.
Stamenkovic, V.R., Mun, B.S., Mayrhofer, K.J., Ross, P.N., Markovic, N.M., 2006. J. Am. Chem. Soc. 128 (27), 8813–8819.
Tamborlane, W.V., Beck, R.W., Bode, B.W., Buckingham, B., Chase, H.P., Clemons, R., Huang, E.S., 2008. N. Engl. J. Med. 359 (14), 1464–1476.
Wang, C., Nie, X.G., Shi, Y., Zhou, Y., Xu, J.J., Xia, X.H., Chen, H.Y., 2017a. ACS Nano 11, 5897–5905.
Wang, D., Xin, H.L., Hovden, R., Wang, H., Yu, Y., Muller, D.A., DiSalvo, F.J., Abruna, H.D., 2013. Nat. Mater. 12, 81–87.
Wang, J., Chen, F., Jin, Y., Johnston, R.L., 2016. J. Mater. Chem. 4, 17828–17837.
Wang, J., Chen, F., Jin, Y., Lei, Y., Johnston, R.L., 2017b. Adv. Funct. Mater. 27, 1700260.
Wang, J., Yang, P., Wei, X., 2015. ACS Appl. Mater. Interfaces 7, 3816–3824.
Wang, L., Li, X., Xue, W., Quan, Z., Qin, X., Wang, F., Xu, X., 2018a. J. Mater. Chem. C 6, 1996–2003.
Wang, L., Zhu, W., Lu, W., Qin, X., Xu, X., 2018b. Biosens. Bioelectron. 111, 41–46.
Welch, C.M., Compton, R.G., 2006. Anal. Bioanal. Chem. 384, 601–619.
Yan, L., Wang, F., Meng, S., 2016. ACS Nano 10, 5452–5458.
Yang, H., He, L.Q., Hu, Y.W., Lu, X., Li, G.R., Liu, B., Ren, B., Tong, Y., Fang, P.P., 2015. Angew. Chem. 54, 11462–11466.
Yang, H., Wang, Z.H., Zheng, Y.Y., He, L.Q., Zhan, C., Lu, X., Tian, Z.Q., Fang, P.P., Tong, Y., 2016. J. Am. Chem. Soc. 138, 16204–16207.
Ye, J.S., Wen, Y., Zhang, W.D., Gan, L.M., Xu, G.Q., Sheu, F.S., 2004. Electrochem. Commun. 6, 66–70.
Yin, Z., Wang, Y., Song, C., Zheng, L., Ma, N., Liu, X., Li, S., Lin, L., Li, M., Xu, Y., Li, W., Hu, G., Fang, Z., Ma, D., 2018. J. Am. Chem. Soc. 140, 864–867.
Zhang, H., Yi, B., Jiang, S., Zeng, Y., Shao, Z., 2017a. ChemElectroChem 4, 1436–1442.
Zhang, J., Qin, X., Torre, B., Zeng, H., Xu, X., 2014. IEEE Trans. Magn. 50 (8), 1–4.
Zhang, L., Jia, C., He, S., Zhu, Y., Wang, Y., Zhao, Z., Gao, X., Zhang, X., Sang, Y., Zhang, D., Xu, X., Liu, H., 2017b. Adv. Sci. 4, 1600448.
Zhang, P., Zeng, G., Song, T., Huang, S., Wang, T., Zeng, H., 2019. Appl. Catal. B Environ. 242, 389–396.
Zhang, X., Wang, G., Liu, X., Wu, J., Li, M., Gu, J., Liu, H., Fang, B., 2008. J. Phys. Chem. C 112 (43), 16845–16849.
Zhang, Y., He, S., Guo, W., Hu, Y., Huang, J., Mulcahy, J.R., Wei, W.D., 2017c. Chem. Rev. 118 (6), 2927–2954.
Zheng, B.Y., Zhao, H., Manjavacas, A., McClain, M., Nordlander, P., Halas, N.J., 2015. Nat. Commun. 6, 7797.
Zheng, Z., Ng, Y.H., Wang, D.W., Amal, R., 2016. Adv. Mater. 28, 9949–9955.
Zhou, L., Swearer, D.F., Zhang, C., Robatjazi, H., Zhao, H., Henderson, L., Dong, L., Christopher, P., Carter, E.A., Nordlander, P., Halas, N.J., 2018. Science 362, 69–72.